

Monolithically Integrated AlGaInAs MQW Polarization Mode Converter Using a Stepped Height Ridge Waveguide

Xiao Sun¹, Shengwei Ye, Weiqing Cheng, Song Liang¹, Member, IEEE, Yongguang Huang¹, Bocang Qiu, Zhibo Li¹, Jichuan Xiong¹, Xuefeng Liu, John H. Marsh¹, Fellow, IEEE, and Lianping Hou¹, Senior Member, IEEE

Abstract—An AlGaInAs multiple-quantum-well (MQW) polarization mode controller (PMC) using a stepped height ridge waveguide is presented, which is monolithically integrated with a sidewall grating distributed feedback laser using quantum well intermixing (QWI). QWI is used to create a 100 nm blueshift in the PMC and to partially eliminate the anisotropy and birefringence of the MQW structure. The PMC structure is modelled and optimized using a 3D full-vectorial Finite-Element Method package. The maximum polarization conversion efficiency (PCE) is around 96% for a 537- μm -long PMC operating at a wavelength of 1550 nm. To maintain a PCE of $\geq 90\%$, the fabrication tolerances of the dry-etch corner and ridge waveguide widths are $\pm 0.05 \mu\text{m}$ and $\pm 0.03 \mu\text{m}$ respectively. The main advantages of the proposed design are that only a single step of MOPVE and two steps of dry etching are required for the whole integrated device, significantly reducing complexity and cost.

Index Terms—Optical polarization, integrated photonic systems, waveguide devices.

I. INTRODUCTION

THE ability to control and manipulate the polarization of light is of increasing importance in a range of applications, for example polarization mode controllers (PMCs) are deployed in long-haul networks to manipulate the TE-TM polarization state of light [1]. Waveguide based PMCs can be integrated with

sources, detectors, and other components in photonic integrated circuits (PICs). An increasing number of devices including polarization-dependent phase shifters (PD-PSs) [2], [3] and laser diodes (LDs) [4] use multiple-quantum-well (MQW) structures as the active region; it is, therefore, desirable to design PMCs compatible with MQW structures. For a polarization tunable source, the integration of the monolithic PMCs waveguides with LDs requires a good transverse mode-match. A PMC based on a particular MQW structure design has been reported that can convert TE- or TM-polarized light into an arbitrarily chosen state of polarization (SOP) [2] albeit with only a 50% TE to TM polarization conversion efficiency (PCE) [3]. The crucial issue for MQW PMCs is the inherent birefringence of the MQW, which disturbs the optimal rotation of the SOP on the Poincaré sphere. Several different material systems and designs have been proposed for PMCs such as GaAs-AlGaAs [5] or InGaSb-AlGaAsSb [6] structures using the reactive ion-etch (RIE) lag phenomenon, InP-InGaAsP structures with a single-trench waveguide [7], angled-facet waveguides [8], two-step waveguides [9] and silicon nanowire PMCs with stepped height ridge waveguides [10], [11]. These PMC devices used bulk material as the core layer in the waveguide and combined a high PCE with a short waveguide length. However, to integrate MQW-based components such as efficient lasers with bulk PMCs, relatively complicated butt-joint PIC techniques involving re-growth are usually used. To simplify the fabrication processes, we have proposed monolithically integrating an InP-AlGaInAs MQW-based sidewall grating distributed-feedback (DFB) laser with an asymmetric half-ridge waveguide PMC [12]. The design used a standard MQW laser structure, with quantum well intermixing (QWI) being used to enlarge the bandgap of the PMC section, reducing the absorption loss, and removing the birefringence associated with the MQW waveguide core. However, because of the thin waveguide core used in standard MQW lasers, the performance of the PMC is very sensitive to the waveguide dimensions and maximizing the power conversion efficiency requires a relatively long (1250 μm) PMC. Both the tight fabrication tolerances and large footprint make this approach unattractive for volume manufacturing.

In this work, an optimized epitaxial design is presented for integrating a monolithic sidewall grating DFB laser with a stepped height ridge waveguide PMC, based on a conventional 1550

Manuscript received February 12, 2022; revised April 22, 2022; accepted May 17, 2022. Date of publication May 20, 2022; date of current version June 7, 2022. This work was supported by U.K. Engineering and Physical Sciences Research Council under Grant EP/R042578/1. (Corresponding author: Xiao Sun.)

Xiao Sun, Shengwei Ye, Weiqing Cheng, John H. Marsh, and Lianping Hou are with the James Watt School of Engineering, University of Glasgow, Glasgow G12 8QQ, U.K. (e-mail: x.sun.2@research.gla.ac.uk; shengwei.ye@glasgow.gla.ac.uk; w.cheng.2@research.gla.ac.uk; ohn.marsh@glasgow.ac.uk; lianping.hou@glasgow.ac.uk).

Song Liang and Yongguang Huang are with the Institute of Semiconductors, Chinese Academy of Sciences, Beijing 100083, China (e-mail: liangs@red.semi.ac.cn; yghuang@semi.ac.cn).

Bocang Qiu is with the Institute of Atomic and Molecular Science, Shaanxi University of Science and Technology, Xian 712081, China (e-mail: qiubc@lumcore.com).

Zhibo Li is with the Fraunhofer Centre for Applied Photonics, Glasgow G11RD, U.K. (e-mail: zhibo.li@fraunhofer.co.uk).

Jichuan Xiong and Xuefeng Liu are with the School of Electronic and Optical Engineering, Nanjing University of Science and Technology, Nanjing 210094, China (e-mail: jichuan.xiong@njust.edu.cn; xuefeng_liu@njust.edu.cn).

Digital Object Identifier 10.1109/JPHOT.2022.3176547

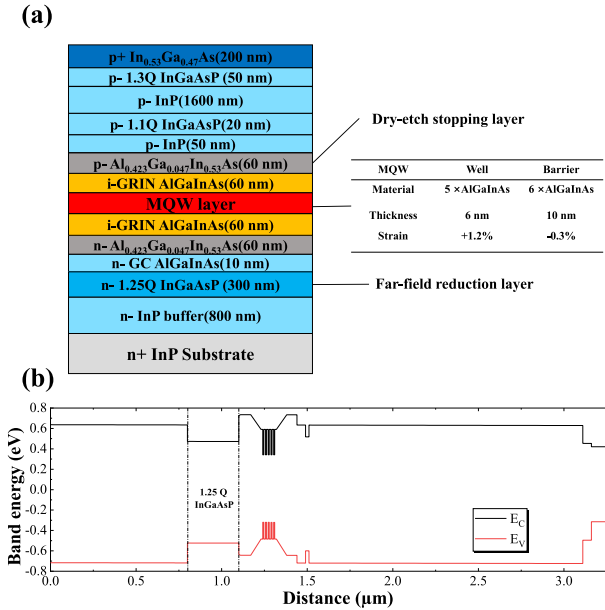


Fig. 1. (a) The epitaxial layer structure of the PMC; (b) Band diagram of the LD-PMC device structure.

nm AlGaInAs/InP MQW LD structure. A thin InGaAsP passive waveguide layer (sometimes known as a far-field reduction layer (FRL) [13]) is embedded below the MQW layer to increase the difference between the propagation constants of the two fundamental modes of the PMC so reducing the half-beat length (L_{π}) and increasing the PCE dramatically. QWI is proposed in the PMC section to blueshift the bandgap absorption edge and minimize waveguide absorption loss [14] and remove the birefringence and material anisotropy associated with the MQW [15]. The top of the AlGaInAs waveguide layer acts as a dry etch stop layer, which allows a critical etch depth to be precisely controlled.

In the following analysis, the PCE of the PMC was optimized and its fabrication tolerances were assessed using the Finite-Element Method (FEM). A maximum PCE of approximately 96% can be achieved in a 537-μm-long AlGaInAs MQW-based PMC.

II. DESIGN AND OPTIMIZATION

The LD-PMC device is based on a commercially available 1550 nm AlGaInAs/InP LD structure [16]. This wafer contains five 6-nm-thick compressively strained (+1.2%) AlGaInAs quantum wells (QWs) and six 10 nm-thick tensile strained (-0.3%) AlGaInAs quantum barriers (QBs). This standard structure is modified by the inclusion of an FRL beneath the waveguide core. The resulting epitaxial layer profile is shown in Fig. 1(a). It comprises an n-InP buffer (800 nm), a 300-nm-thick n-InGaAsP FRL with a bandgap wavelength of 1.25 μm (1.25Q), and an n-type graded-composition (GC) AlGaInAs layer (10 nm). The MQW layer is sandwiched by two 60-nm-thick graded-index separate confinement heterostructure (GRINSCH) AlGaInAs layers whose Al compositions are graded from 0.42 to 0.34, and two 60-nm-thick AlGaInAs waveguide layers. The

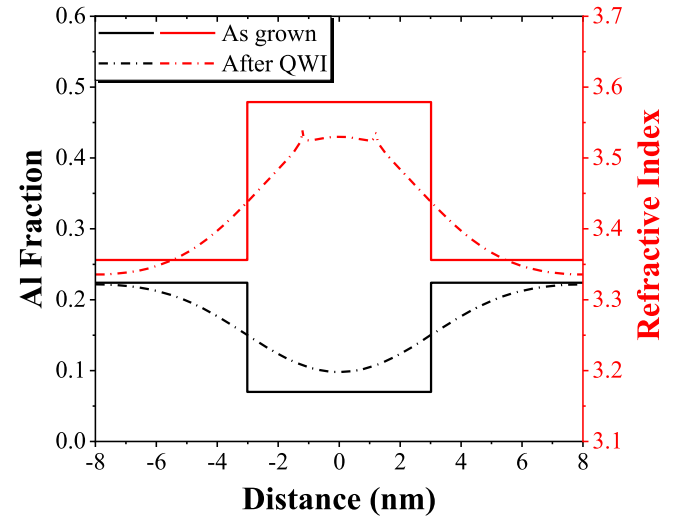


Fig. 2. Al fraction and reflective index distribution at 1550 nm wavelength through one MQW period for as-grown and after QWI by 100 nm blueshift.

upper of these also act as a dry etch stop layer. The structure is completed with 50 nm of p-InP, 20 nm of InGaAsP (1.1Q), 1.6 μm of p-InP cladding, and 50 nm of p-InGaAsP (1.3Q), and a 200-nm-thick p+ InGaAs contact layer. Metal-organic vapour phase epitaxy (MOVPE) is used to grow this structure on a sulfur-doped InP substrate. Fig. 1(b) shows the band diagram of the LD-PMC device. Because of quantum mechanical selection rules, the compressive strain in the AlGaInAs QWs results in TE-polarized laser operation.

QWI is a technique for selectively tuning the quantum well bandgap across a wafer postgrowth. After intermixing, the MQW structure has comparable characteristics to those of a bulk layer, and its material anisotropy vanishes [15]. In order to calculate the optical properties of QWI-processed material, we have used Fick's law of diffusion to model the QW profile [17] and its PL spectrum during intermixing. In the model, the degree of intermixing is represented by the diffusion length on the group III substance, $C(z, L_D)$, as shown in (1):

$$C(z, L_D) = (C_1 - C_2) \left[1 - \frac{1}{2} \operatorname{erf} \left(\frac{z - \frac{L_W}{2}}{2\sqrt{L_D}} \right) + \frac{1}{2} \operatorname{erf} \left(\frac{z + \frac{L_W}{2}}{2\sqrt{L_D}} \right) \right] \quad (1)$$

where C_1 and C_2 are the initial atomic mole fractions for QW and QB materials respectively, z is the quantization direction along the growth axis (QW centered at $z = 0$), and "erf" denotes the error function, L_W is the quantum well width, and L_D is the diffusion length. The experimental and calculated bandgap shifts can be fitted by an appropriate choice of L_D . Fig. 2 shows the calculated Al fraction profile and refractive index for both the as-grown structure and intermixed material where the QW bandgap was blue-shifted by 100 nm, corresponding to an Al atom diffusion length of 1.53 nm. At the interfaces between the intermixed wells and barriers, the refractive index curve has been smooth rather than stepped transitions. It is noticeable that there are two spikes in the refractive index profile

TABLE I
CRITICAL AS-GROWN MQW STRUCTURAL CHARACTERISTICS AND AFTER
100 nm QWI BANDGAP WIDENING

	PL wavelength	Al fraction	Refractive Index	Diffusion Length
As grown	1530 nm	0.070 (QW)	3.579 (QW)	
		0.224 (QB)	3.356 (QB)	
After QWI	1430 nm	0.166(average)	3.4162(average)	1.53 nm

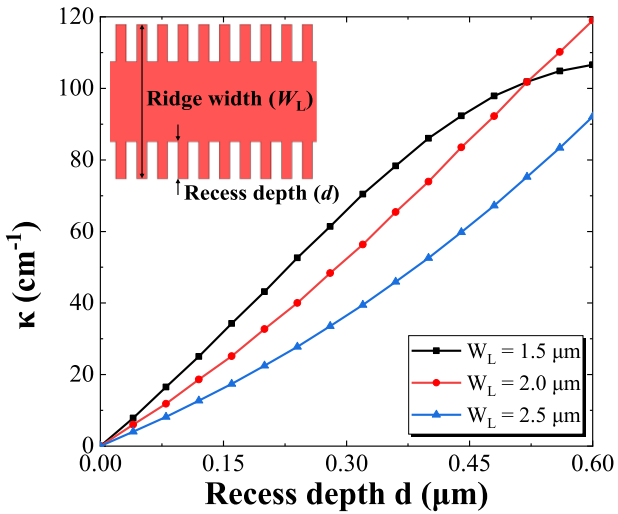


Fig. 3. Sidewall grating coupling coefficient κ as the grating recess depth d , for ridge waveguide widths $W_L = 2.5, 2.0$ and $1.5 \mu\text{m}$.

of the intermixed quantum well, which is due to the effect of resonance absorption at which the photon energy is equal to the bandgap of materials, and the birefringence associated with the MQW is partially eliminated. The refractive index of each epitaxial layer is derived from the Adachi model [18], [19], which was developed for energies close to the bandgap. Other critical characteristics of the MQW before and after QWI are shown in Table I. The detailed process of QWI can be referred to [14].

Fig. 3 shows the dependence of coupling coefficient κ with grating recess depth d for a ridge waveguide height at $1.92 \mu\text{m}$, with laser ridge waveguide widths $W_L = 2.5, 2.0$ and $1.5 \mu\text{m}$. It is found that the coupling coefficient κ can reach $90/\text{cm}$ for $d = 0.6 \mu\text{m}$ and $W_L = 2.5 \mu\text{m}$. Compared with the results of the $80/\text{cm}$ for the wafer structure without 300-nm 1.25Q InGaAsP layer, a $10/\text{cm}$ increase for the κ value, which is enough for the $600 \mu\text{m}$ long sidewall grating DFB laser [20]. The monolithic LD-PMC device is depicted in Fig. 4(a). It consists of a $2.5\text{-}\mu\text{m}$ -wide ridge waveguide AlGaInAs DFB laser operating at 1550 nm , a $50\text{-}\mu\text{m}$ -long taper interconnection, and two symmetric input and output ridge waveguides separated by the stepped height ridge waveguide PMC. Fig. 4(b) presents cross-section views of the input/output waveguide and the PMC. Here W_0 and W are the widths of the ridge waveguide and dry-etch corner, and D_0 and D are their dry-etched depths respectively. The etched depth D can be precisely controlled because the top 60 nm thick AlGaInAs waveguide layer acts as a dry etch stop layer

when using $\text{CH}_4/\text{H}_2/\text{O}_2$ RIE recipe. The value of D is set at $1.92 \mu\text{m}$, and D_0 was set at $3.3 \mu\text{m}$. Modelling shows that when $D_0 \geq 3.3 \mu\text{m}$, the etch depth D_0 has no influence on the eigenmode profiles. The ridge waveguide width, W_0 , can be defined using the high resolution of the ebeam lithography (EBL). Hence, the PCE is only sensitive to the width W of the dry-etch corner. The light from the laser is TE-polarized, so at the input of the PMC, the power fractions in the fundamental TE_0 and TM_0 modes shown in Fig. 4(c) are 100% and 0% respectively. According to [21], to achieve the maximum TE-TM conversion efficiency, the eigenmodes (TE_0 and TM_0) axes of the asymmetric PMC waveguide should be rotated in the diagonal direction (45° rotation) with respect to the input straight waveguide (see Fig. 4(b)), which means the TE-polarized power fraction in both TE_0 and TM_0 profiles presented in Fig. 4(d) is 50%. After propagating a half-beat length $L_\pi = \pi/(|\beta_1 - \beta_2|)$ (where β_1 and β_2 are the propagation constants of the TE_0 and TM_0 modes), the polarization is rotated 90° , and the output becomes TM-polarized. Hence, this design primarily requires optimizing the widths W_0 and W to achieve a 45° rotation of TE_0 and TM_0 .

In the following optimization of the PCE dimensions, a 3D full-vectorial modal analysis was implemented using the EME (Eigenmode Expansion) solver. The EME solver collected 100 data points of the PMC geometry by splitting the starting range of W and W_0 into 10 grids in this optimization step. A self-written script that connects to the results of the EME Solver calculation was employed to automatically allow the solver to calculate the PCE of all the waveguide structure data points with the PMC length being the corresponding half-beat length (L_π).

III. SIMULATION AND RESULTS

Since the PMC waveguide must support only the fundamental TE_0 and TM_0 modes, the corresponding range of the ridge waveguide widths (W_0) must first be found. The effective modal index (N_{eff}) values for the first four modes ($\text{TE}_0, \text{TM}_0, \text{TE}_1, \text{TM}_1$) were calculated using the FDE Solver and are presented in Fig. 5. These results indicate that for $1.0 \mu\text{m} \leq W_0 \leq 2.0 \mu\text{m}$, only the TE_0 and TM_0 modes are supported. Following this stage, the range of W_0 was set between $1.0 \mu\text{m}$ and $1.8 \mu\text{m}$ and W between $0.2 \mu\text{m}$ and $0.7 \mu\text{m}$ in the EME Solver to find the dimensions that maximize the PCE. The PCE definition can be referred to in (2) in [5]:

$$PCE = \frac{P_{TM}}{P_{TM} + P_{TE}} \times 100\% \quad (2)$$

where P_{TM} and P_{TE} are the TM and TE output powers respectively. Fig. 6(a) shows a contour plot of the maximum PCE. The PCE is greater than 80% in the region $1.30 \mu\text{m} \leq W_0 \leq 1.45 \mu\text{m}$ and $0.35 \mu\text{m} \leq W \leq 0.60 \mu\text{m}$. Hence, a further simulation over a narrower range of W_0 and W was undertaken, and these results are shown in Fig. 6(b). The final optimum dimensions of the PMC waveguide chosen here are $W_0 = 1.42 \mu\text{m}$ and $W = 0.415 \mu\text{m}$, representing a compromise offering high PCE (96%) and short L_π ($537 \mu\text{m}$) (see Fig. 6(c)). The modal profiles of this optimum PMC waveguide were presented

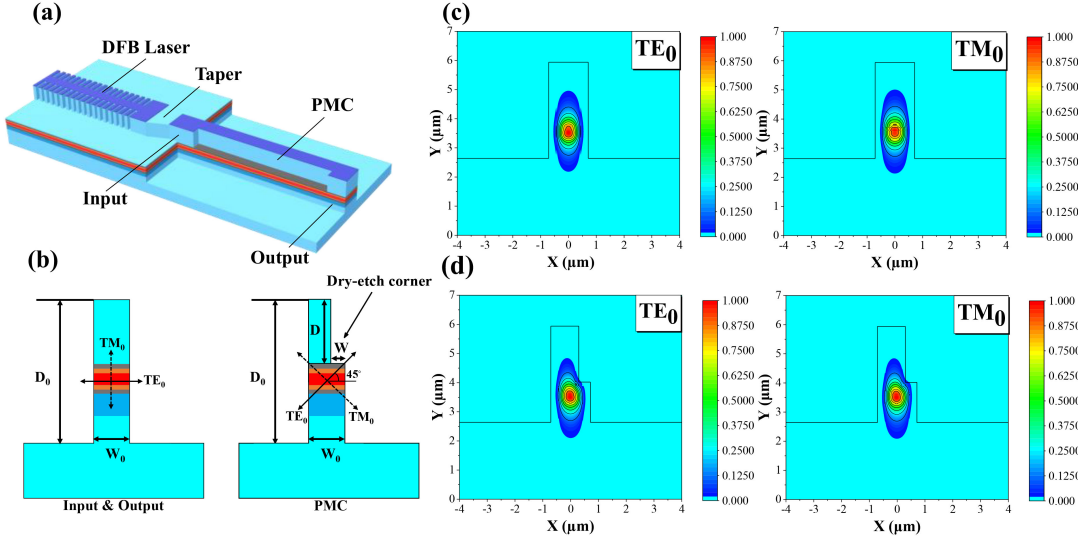


Fig. 4. (a) Monolithic LD-PMC device. (b) Cross-section of the input/output waveguides (left) and PMC waveguide (right). (c) The two fundamental eigenmodes TE₀ and TM₀ profile in the input section ($W_0 = 1.42 \mu\text{m}$, $D_0 = 3.3 \mu\text{m}$). (d) TE₀ and TM₀ profiles in the PMC ($W_0 = 1.42 \mu\text{m}$, $W = 0.415 \mu\text{m}$, $D_0 = 3.3 \mu\text{m}$).

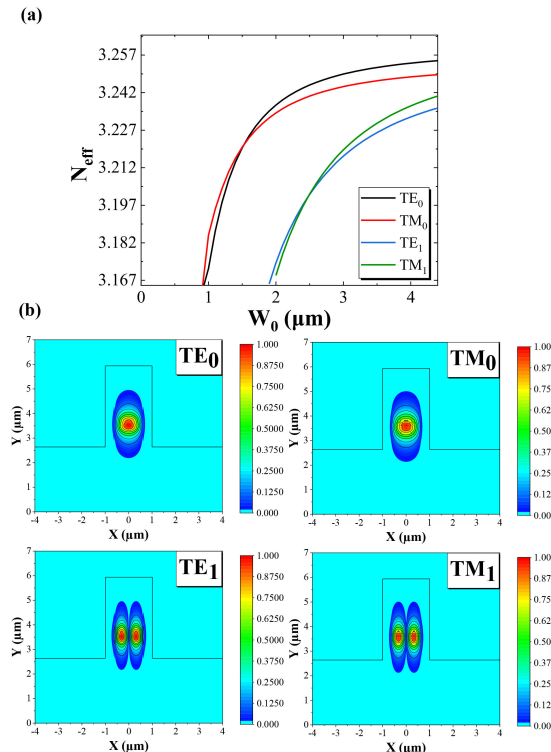


Fig. 5. (a) Calculated waveguide N_{eff} of the TE₀, TM₀, TE₁, TM₁ modes as a function of the ridge waveguide width W_0 . (b) Simulated TE₀ and TM₀, TE₁ and TM₁ mode profiles for a ridge waveguide width (W_0) of $2.1 \mu\text{m}$ and height (D_0) of $3.3 \mu\text{m}$.

In Fig. 4(d), the calculated effective modal indexes (N_{eff}) of the fundamental TE₀ and TM₀ modes are 3.210244 and 3.20880 respectively. Fig. 7(a) shows the N_{eff} and effective modal indexes difference ΔN_{eff} of the TE₀, TM₀ modes ($\Delta N_{\text{eff}} = N_{\text{eff}}(\text{TE}_0) - N_{\text{eff}}(\text{TM}_0)$) as the function of the FRL thickness T . T starts from $0.1 \mu\text{m}$ because there is no transverse eigenmode when $T < 0.097 \mu\text{m}$. These results indicate that for $T \geq 0.1 \mu\text{m}$, the

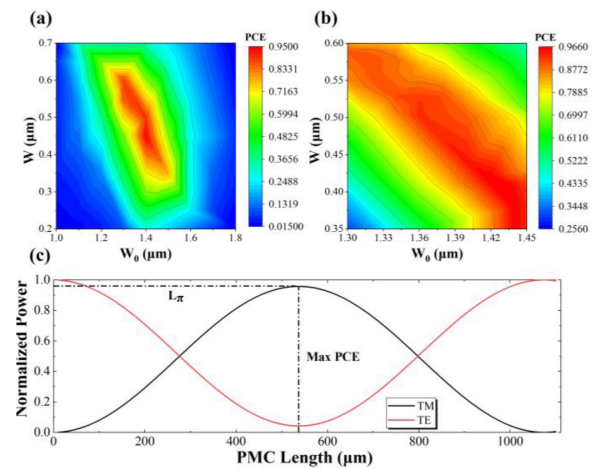


Fig. 6. (a) Broad-range optimization of PCE as a function of waveguide width (W_0) and corner width (W), (b) Narrow-range optimization, (c) Relative powers in TE₀ and TM₀ modes as a function of PMC length simulated by EME Solver.

TE₀ and TM₀ modes are maintained and at $T = 0.375 \mu\text{m}$ the minimum of ΔN_{eff} is 0.00128. Fig. 7(b) presents the PCE and half-beat length (L_{π}) as the function of T for the optimum PMC dimensions of $W_0 = 1.42 \mu\text{m}$, $W = 0.415 \mu\text{m}$ and $L_{\text{PMC}} = 537 \mu\text{m}$ from the aforementioned narrow-range optimization results. It is indicated that when the FRL thickness is set at $0.3 \mu\text{m}$, the highest PCE (96%) is obtained with a relevant short L_{π} ($537 \mu\text{m}$). Therefore, a 300 nm thick FRL represents a good balance between PCE and L_{π} .

IV. TOLERANCE ANALYSIS

Since process variability in the fabrication of real devices causes uncertainty in the values of W and W_0 , the fabrication tolerances need to be investigated. In this calculation, the length of the PMC (L_{PMC}) is fixed at $537 \mu\text{m}$ and waveguide deep-etch depth (D_0) at $3.3 \mu\text{m}$. Fig. 8(a) shows the variation of the

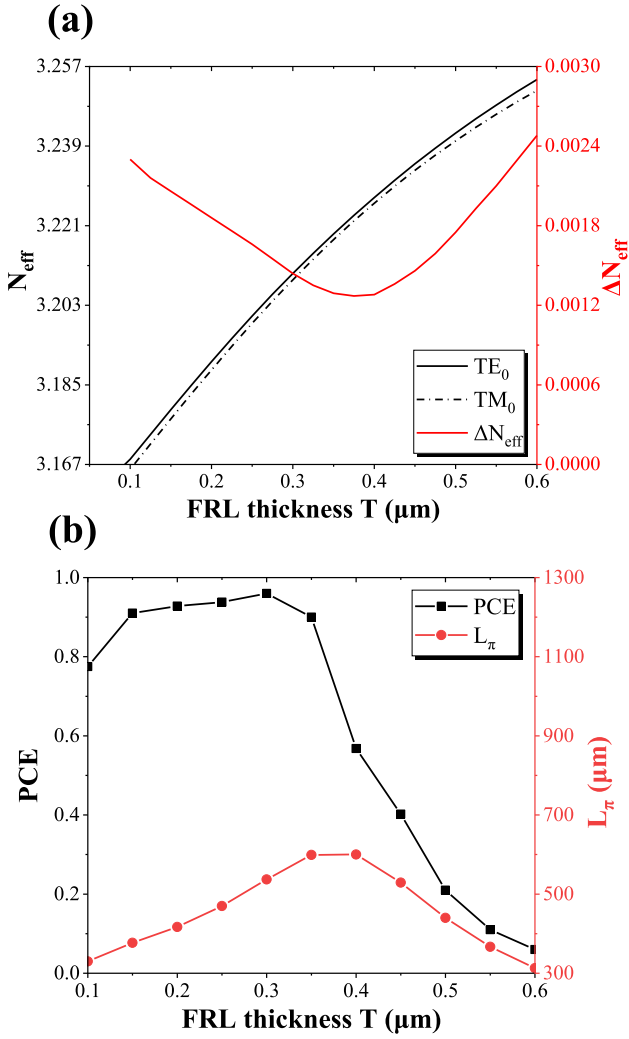


Fig. 7. (a) Calculated waveguide N_{eff} and refractive index difference ΔN_{eff} of the TE₀, TM₀ modes as a function of the FRL thickness T . (b) Variation of PCE and L_π as a function of FRL thickness T ($W = 1.42 \mu\text{m}$, $W_0 = 0.415 \mu\text{m}$ and $L_{\text{PMC}} = 537 \mu\text{m}$).

PCE as a function of the dry-etch corner width (W) for three different ridge waveguide widths (W_0). For the optimum value of waveguide width, $W_0 = 1.42 \mu\text{m}$, the PCE decreases by 6.25% over the range of corner width, $W = 0.415 \pm 0.05 \mu\text{m}$. It also can be seen that a deviation of $\pm 0.02 \mu\text{m}$ in W_0 causes a 3.9% reduction of PCE for the optimum waveguide width $W = 0.415 \mu\text{m}$. In Fig. 8(b), where the results of sweeping W_0 are presented, W_0 varying over the range $1.42 \pm 0.03 \mu\text{m}$ results in the PCE decreasing by up to 6.8%. Fig. 8(c) presents the conversion efficiency as a function of dry-etch corner depth (D) for $W_0 = 1.42 \mu\text{m}$ and $W = 0.415 \mu\text{m}$. There is a 16% decrease in PCE for a deviation of $\pm 0.05 \mu\text{m}$ from the optimum D of $1.92 \mu\text{m}$. This result reveals the importance of having an AlGaInAs dry-etch-stop layer in the PMC design. During RIE using a CH₄/H₂/O₂ gas mixture, the etch rate on InP is about 40 nm/min, while the rate on AlInGaAs was only about 1 nm/min [22]. As a result, the top AlGaInAs waveguide layer acts as an efficient etch-stop layer with a selectivity of over 40:1 when compared to InP. Fig. 8(d) presents the PCE with respect to wavelength.

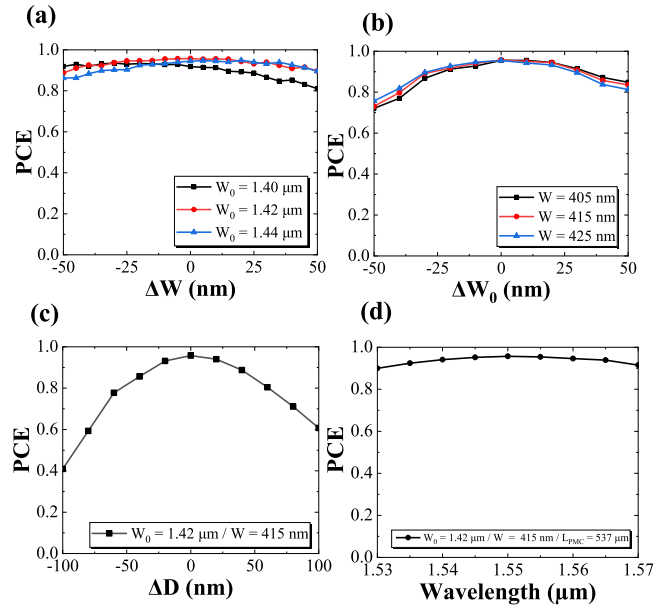


Fig. 8. (a) Variation of PCE as a function of dry-etch corner width W (optimal $W = 0.415 \mu\text{m}$ for $W_0 = 1.40 \mu\text{m}$, $1.42 \mu\text{m}$ and $1.44 \mu\text{m}$, $L_{\text{PMC}} = 537 \mu\text{m}$). (b) PCE with respect to waveguide width W_0 (optimal $W_0 = 1.42 \mu\text{m}$ for $W = 0.405 \mu\text{m}$, $0.415 \mu\text{m}$ and $0.425 \mu\text{m}$, $L_{\text{PMC}} = 537 \mu\text{m}$). (c) PCE with respect to dry-etch corner depth D ($W_0 = 1.42 \mu\text{m}$, $W = 0.415 \mu\text{m}$ and $L_{\text{PMC}} = 537 \mu\text{m}$). (d) Wavelength dependence of PCE ($W = 1.42 \mu\text{m}$, $W_0 = 0.415 \mu\text{m}$ and $L_{\text{PMC}} = 537 \mu\text{m}$).

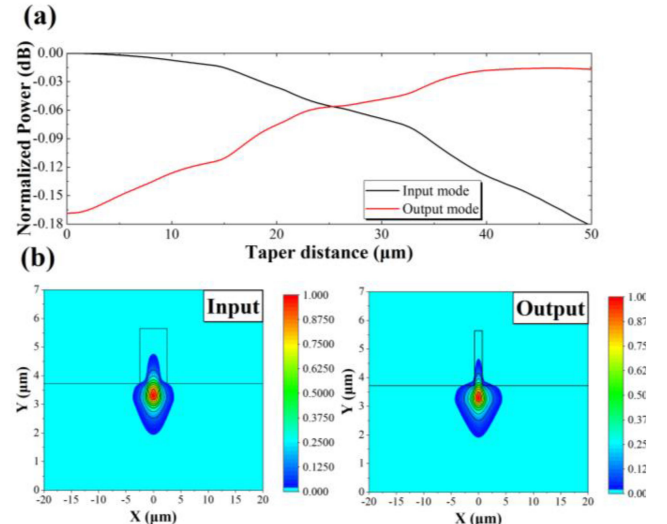


Fig. 9. (a) Normalized power as a function of taper distance for input and output mode. (b) Input and output mode profiles of taper.

operating wavelength for the optimum PMC dimensions of $W_0 = 1.42 \mu\text{m}$, $W = 0.415 \mu\text{m}$ and $L_{\text{PMC}} = 537 \mu\text{m}$. The PCE exceeds 90% over the entire C-band (1530–1565 nm). According to [23], the waveguide losses (α) of a 2.5-μm-wide shallow etched ridge waveguide, with a blue-shifted bandgap of 100 nm, were found to be 4.1 /cm and 2.0 /cm for the TE and TM modes respectively, measured by the Fabry-Perot fringe method at a wavelength of 1550 nm [24]. The excess loss for a 537-μm-long PMC at 1550 nm wavelength was calculated to be around 0.97

dB. This consists of a 0.02 dB transfer loss in the 50- μm -long taper calculated using the EME Solver as illustrated in Fig. 9, and a 0.95 dB propagation loss owing to the deeply etched ridge waveguide [25].

V. CONCLUSION

The design of a monolithically integrated 1550 nm PMC and DFB LD has been proposed and optimized. The epitaxial structure includes an FRL to reduce the length of the PMC section. The PMC uses a stepped height ridge waveguide, and the DFB laser uses a sidewall grating. QWI is used in the PMC to enlarge the bandgap to minimize absorption loss and partially remove birefringence and material anisotropy associated with the MQW. We also evaluated the fabrication tolerances of the TE-TM PCE using Finite-Element modelling. The optimized PMC design offers a PCE of 96% using a 537- μm -long stepped height ridge waveguide, with a ridge waveguide width and depth of 1.42 μm and 3.30 μm , and dry-etch corner width and depth of 0.415 μm and 1.92 μm . The tolerances of the dry-etch corner and ridge waveguide widths are $\pm 0.05 \mu\text{m}$ and $\pm 0.03 \mu\text{m}$ respectively for a PCE deviation of less than 7%. The PCE was calculated for wavelengths from 1530 to 1565 nm and always exceeded 90%. The insertion loss of the PMC was estimated to be around 0.97 dB at a wavelength of 1550 nm. The main advantage of the proposed design is the capability of using only a single MOPVE step and implementing the fabrication process with only two dry-etch steps, significantly reducing complexity and cost.

ACKNOWLEDGMENT

The authors would like to acknowledge the staff of the James Watt Nanofabrication Centre at the University of Glasgow for help in fabricating the devices and Dr. Shengwen Xie for his help with the Finite-Element Method simulation.

REFERENCES

- [1] K. Kikuchi, "Fundamentals of coherent optical fiber communications," *J. Lightw. Technol.*, vol. 34, no. 1, pp. 157–179, Jan. 2016.
- [2] M. Ito *et al.*, "Efficient InGaAsP MQW-based polarization controller without active-passive integration," *Opt. Exp.*, vol. 29, no. 7, pp. 10538–10545, 2021.
- [3] D. C. Hutchings and B. M. Holmes, "A waveguide polarization toolset design based on mode beating," *IEEE Photon. J.*, vol. 3, no. 3, pp. 450–461, Jun. 2011.
- [4] B. Holmes, M. Naeem, D. Hutchings, J. Marsh, and A. Kelly, "A semiconductor laser with monolithically integrated dynamic polarization control," *Opt. Exp.*, vol. 20, no. 18, pp. 20545–20550, 2012.
- [5] B. Holmes and D. Hutchings, "Realization of novel low-loss monolithically integrated passive waveguide mode converters," *IEEE Photon. Technol. Lett.*, vol. 18, no. 1, pp. 43–45, Jan. 2006.
- [6] S. Xie, S. M. Andersson, S. Ye, Z. Niu, J. H. Marsh, and L. Hou, "Design of 2 μm wavelength polarization mode controllers," in *Proc. Int. Conf. U.K.-China Emerg. Technol.*, 2020, pp. 1–3.
- [7] S.-H. Kim, R. Takei, Y. Shoji, and T. Mizumoto, "Single-trench waveguide TE-TM mode converter," *Opt. Exp.*, vol. 17, no. 14, pp. 11267–11273, 2009, doi: [10.1364/OE.17.011267](https://doi.org/10.1364/OE.17.011267).
- [8] U. Khalique *et al.*, "Ultrashort polarization converter on InP/InGaAsP fabricated by optical lithography," in *Proc. Integr. Photon. Res. Appl./Nanophotonics Inf. Syst.*, San Diego, CA, USA, 2005, Paper IWA3. [Online]. Available: <http://www.osapublishing.org/abstract.cfm?URI=IPRA-2005-IWA3>
- [9] C. Alonso-Ramos *et al.*, "Polarization rotator for InP rib waveguide," *Opt. Lett.*, vol. 37, no. 3, pp. 335–337, 2012.
- [10] Z. Wang and D. Dai, "An ultrasmall polarization rotator based on Si nanowire," in *Proc. Asia Opt. Fiber Commun. Optoelectron. Conf.*, 2007, pp. 567–569.
- [11] M. Aamer *et al.*, "CMOS compatible silicon-on-insulator polarization rotator based on symmetry breaking of the waveguide cross section," *IEEE Photon. Technol. Lett.*, vol. 24, no. 22, pp. 2031–2034, Nov. 2012.
- [12] X. Sun *et al.*, "Design and optimization of 1.55 μm AlGaInAs MQW polarization mode controllers," *Photonics*, vol. 8, no. 10, pp. 422–432, 2021.
- [13] B. Qiu, O. Kowalski, S. McDougall, B. Schmidt, and J. H. Marsh, "High-performance red lasers with low beam divergence," *IEEE Photon. J.*, vol. 1, no. 3, pp. 172–177, Sep. 2009.
- [14] L. Hou, M. Hajji, R. Dylewicz, B. Qiu, and A. C. Bryce, "Monolithic 45-GHz mode-locked surface-etched DBR laser using quantum-well intermixing technology," *IEEE Photon. Technol. Lett.*, vol. 22, no. 14, pp. 1039–1041, Jul. 2010.
- [15] Y. Suzuki, H. Iwamura, T. Miyazawa, A. Wakatsuki, and O. Mikami, "Polarization-dependent refractive-index change induced by superlattice disordering," *IEEE J. Quantum Electron.*, vol. 32, no. 11, pp. 1922–1931, Nov. 1996.
- [16] L. Hou *et al.*, "Subpicosecond pulse generation at Quasi-40-GHz using a passively mode-locked AlGaInAs-InP 1.55- μm strained quantum-well laser," *IEEE Photon. Technol. Lett.*, vol. 21, no. 23, pp. 1731–1733, Dec. 2009.
- [17] J. Crank, *The Mathematics of Diffusion*. Oxford, U. K.: Oxford Univ. Press, 1979.
- [18] S. Adachi, *Physical Properties of III-V Semiconductor Compounds*. Hoboken, NJ, USA: Wiley, 1992.
- [19] M. Guden and J. Piprek, "Material parameters of quaternary III-V semiconductors for multilayer mirrors at wavelength," *Modelling Simul. Mater. Sci. Eng.*, vol. 4, no. 4, pp. 349–357, 1996.
- [20] L. Hou, M. Tan, M. Hajji, I. Eddie, and J. H. Marsh, "EML based on sidewall grating and identical epitaxial layer scheme," *IEEE Photon. Technol. Lett.*, vol. 25, no. 12, pp. 1169–1172, Jun. 2013.
- [21] H. Deng, D. O. Yevick, C. Brooks, and P. E. Jessop, "Design rules for slanted-angle polarization rotators," *J. Lightw. Technol.*, vol. 23, no. 1, pp. 432–445, 2005. [Online]. Available: <http://www.osapublishing.org/jlt/abstract.cfm?URI=jlt-23-1-432>
- [22] S. Fürst, M. Sorel, A. Scirè, G. Giuliani, and S. Yu, "Technological challenges for CW operation of small-radius semiconductor ring lasers," in *Proc. Semicond. Lasers Laser Dyn. II*, 2006, Art. no. 61840R.
- [23] L. Hou, M. Hajji, J. Akbar, J. H. Marsh, and A. C. Bryce, "AlGaInAs/InP monolithically integrated DFB laser array," *IEEE J. Quantum Electron.*, vol. 48, no. 2, pp. 137–143, Feb. 2012.
- [24] R. Walker, "Simple and accurate loss measurement technique for semiconductor optical waveguides," *Electron. Lett.*, vol. 21, no. 13, pp. 581–583, 1985.
- [25] H. El-Refai, D. Yevick, and T. Jones, "Slanted-rib waveguide InGaAsP-InP polarization converters," *J. Lightw. Technol.*, vol. 22, no. 5, pp. 1352–1357, 2004.